International Journal of Modern Engineering and Management | IJMEM
ISSN No: 3048-8230
Volume 3 Issue 6 June 2026

Synthesis, Characterisation and Electrochemical Performance of Reduced Graphene Oxide–Metal Oxide Nanocomposite Electrodes for High-Energy Supercapacitor Applications

Vikram Singh Chauhan,, **Arunabha Ghosh**, **Deepak Ranjan Sahoo**

Department of Chemical Engineering, Biju Patnaik Institute of Technology, Rourkela, Odisha, India
Department of Materials Engineering, Himachal Pradesh Institute of Engineering and Technology, Shimla, Himachal Pradesh, India

Abstract

Electrochemical double-layer capacitors and pseudocapacitors — collectively termed supercapacitors — occupy a critical niche in the energy storage landscape between conventional dielectric capacitors and rechargeable batteries, offering higher power density than batteries and higher energy density than capacitors. The primary limitation constraining supercapacitor deployment in electric vehicle regenerative braking systems and grid-scale pulse power applications is the insufficient energy density (typically 5–10 Wh/kg for carbon-based electrodes) relative to lithium-ion batteries (150–250 Wh/kg). Reduced graphene oxide (rGO), produced by chemical or thermal reduction of graphene oxide, provides a high-surface-area conducting scaffold (theoretical surface area 2630 m²/g) that supports pseudocapacitive metal oxide nanoparticles whose Faradaic redox reactions dramatically increase charge storage capacity beyond the pure electrical double-layer mechanism available to carbon-only electrodes. This study synthesises rGO/metal oxide nanocomposite electrodes incorporating MnO_2, NiO, and Co_3O_4 nanoparticles by hydrothermal co-deposition, comprehensively characterises them by XRD, FTIR, Raman spectroscopy, SEM-EDX, BET surface area analysis, and electrochemical techniques including cyclic voltammetry (CV), galvanostatic charge-discharge (GCD), and electrochemical impedance spectroscopy (EIS), and evaluates their cycling stability over 5000 charge-discharge cycles. The rGO/MnO_2 composite achieves the highest specific capacitance of 412 F/g at 1 A/g with energy density of 45.8 Wh/kg and power density of 0.31 kW/kg, retaining 87.4% capacitance after 5000 cycles. BET analysis confirms systematic increase in accessible surface area from 186 m²/g (neat rGO) to 312 m²/g (rGO/MnO_2). EIS reveals a charge transfer resistance of 1.2 Ω for rGO/MnO_2, confirming low interfacial impedance that underpins high rate capability.

Keywords: *supercapacitor, reduced graphene oxide, manganese dioxide, nickel oxide, cobalt oxide, hydrothermal synthesis, cyclic voltammetry, electrochemical impedance spectroscopy, energy density, cycling stability*

1. Introduction

The global transition toward renewable energy sources — photovoltaic, wind, and tidal generation — introduces intermittency into electrical grids that were designed around dispatchable fossil fuel generation, creating an acute demand for electrochemical energy storage systems capable of rapid charge-discharge cycling, high cycle life, and wide operating temperature range. Supercapacitors have attracted substantial research attention as complementary storage elements to batteries in hybrid storage architectures, where the supercapacitor handles high-power transients (vehicle acceleration, regenerative braking pulses, frequency regulation events) while the battery provides sustained energy delivery. The fundamental electrochemical distinction between supercapacitors and batteries lies in the charge storage mechanism: supercapacitors store charge electrostatically at the electrode-electrolyte interface (electric double layer) or through fast, near-surface Faradaic reactions (pseudocapacitance), whereas batteries involve bulk-phase ion intercalation or conversion reactions. This distinction confers supercapacitors' characteristic advantages: power densities of 1–10 kW/kg (10–100 times higher than batteries), cycle lives of 100,000–1,000,000 cycles (versus 500–5000 for batteries), and charging times of seconds to minutes.

The principal challenge in supercapacitor electrode materials research is bridging the energy density gap with batteries while preserving the power density and cycle life advantages. Activated carbon, the current commercial electrode material, achieves specific capacitances of 100–200 F/g in aqueous electrolytes — adequate for cycle life but insufficient for competitive energy density. Graphene-based materials offer a theoretical pathway to dramatically higher capacitance: pristine graphene's theoretical specific capacitance of approximately 550 F/g, if achievable in practice, would yield energy densities of 60–85 Wh/kg competitive with lead-acid batteries. Practical rGO electrodes achieve 100–300 F/g due to sheet restacking that reduces accessible surface area from the theoretical maximum. Metal oxide pseudocapacitive materials — RuO_2, MnO_2, NiO, Co_3O_4, V_2O_5 — achieve much higher specific capacitances (400–2000 F/g for some materials) through multi-electron Faradaic reactions but suffer from poor electrical conductivity, low surface area utilisation, and mechanical degradation during volume changes accompanying redox cycling. Compositing metal oxide nanoparticles with rGO scaffolds addresses both limitations simultaneously: the rGO provides electrical conductivity and prevents metal oxide particle agglomeration, while the metal oxide provides pseudocapacitive charge storage that dramatically amplifies the composite electrode's capacitance relative to rGO alone.

Among transition metal oxides investigated as rGO composite partners, MnO_2 has attracted the greatest attention due to its high theoretical capacitance (1370 F/g), low cost, natural abundance, and environmental benignity. NiO offers theoretical capacitance of approximately 2584 F/g through the $Ni(OH)_2$/NiOOH redox couple but is limited by poor rate capability in many electrolyte systems. Co_3O_4 has emerged as a promising intermediate — theoretical capacitance 3560 F/g — with relatively good electronic conductivity among the transition metal oxides. A comparative systematic investigation of all three metal oxides under identical synthesis and testing conditions, using the same rGO scaffold and electrolyte, has not been extensively reported in the Indian literature, where most studies examine individual composites without the controlled comparative framework needed to guide industrial materials selection. The present study addresses this gap by fabricating rGO/MnO_2, rGO/NiO, and rGO/Co_3O_4 composites by a unified hydrothermal synthesis protocol and subjecting all four electrodes (including neat rGO) to an identical electrochemical characterisation battery.

This research was initiated as a collaborative project between five institutions across northern, eastern, and central India, with authors contributing expertise in electrode fabrication, electrochemical characterisation, surface analysis, and materials characterisation. The collaborative framework was motivated by the complementary infrastructure available at different partner institutions, enabling comprehensive characterisation not achievable at any single laboratory, and by the shared scientific goal of advancing India's domestic supercapacitor materials capability in support of national electric vehicle and grid storage programmes.

2. Materials and Methods

2.1 Synthesis of Graphene Oxide and Reduced Graphene Oxide

Graphene oxide (GO) was prepared from natural graphite flakes (99.9% purity, Sigma-Aldrich) by a modified Hummers method. Graphite (2 g) was added to a mixture of concentrated H_2SO_4 (46 mL) and $NaNO_3$ (1 g) in an ice bath, followed by slow addition of $KMnO_4$ (6 g) maintaining temperature below 10°C. The mixture was stirred at 35°C for 2 hours, diluted with deionised water (92 mL), then treated with 30% H_2O_2 solution (10 mL) until bubbling ceased. The resulting GO suspension was washed by repeated centrifugation with 5% HCl solution and deionised water until the supernatant pH reached 6–7, then freeze-dried to produce GO powder. Reduced graphene oxide was obtained by chemical reduction: GO was dispersed in deionised water (1 mg/mL) by probe sonication, hydrazine hydrate (1 µL per mg GO) was added, and the suspension was heated at 95°C for 1 hour under nitrogen atmosphere. The resulting rGO was filtered, washed thoroughly, and dried at 60°C.

2.2 Hydrothermal Synthesis of rGO/Metal Oxide Composites

Three composite materials were synthesised by hydrothermal co-deposition. For rGO/MnO_2: GO (50 mg) was dispersed in deionised water (40 mL), $KMnO_4$ (200 mg) was added, and the mixture was transferred to a 50 mL Teflon-lined autoclave and heated at 160°C for 12 hours. The autoclave was cooled to room temperature, and the product was collected by filtration, washed with deionised water and ethanol, and dried at 80°C. The hydrothermal conditions simultaneously reduced GO to rGO and deposited MnO_2 nanoparticles on the graphene surface. For rGO/NiO: a mixture of GO (50 mg), $Ni(NO_3)_2 \cdot 6H_2O$ (290 mg), and urea (300 mg) in 40 mL water was processed under identical hydrothermal conditions (180°C, 10 hours), with subsequent calcination at 300°C for 2 hours in air to convert $Ni(OH)_2$ to NiO while preserving the rGO scaffold. For rGO/Co_3O_4: $Co(NO_3)_2 \cdot 6H_2O$ (290 mg) replaced the nickel salt with otherwise identical synthesis conditions, with calcination at 250°C.

2.3 Electrode Preparation and Electrochemical Testing

Working electrodes were fabricated by mixing active material (80 wt%), conductive carbon black (10 wt%), and polyvinylidene fluoride binder (10 wt%) in N-methyl-2-pyrrolidinone solvent to form a homogeneous slurry, which was coated onto nickel foam current collector (1×1 cm^2 area) and dried at 120°C under vacuum for 12 hours. The mass loading of active material was maintained at 3.0±0.1 mg/cm^2 across all electrodes. Electrochemical measurements were performed in a standard three-electrode cell configuration in 6 M KOH aqueous electrolyte, using Ag/AgCl reference electrode and platinum wire counter electrode, controlled by a BioLogic SP-150 potentiostat/galvanostat. Cyclic voltammetry was conducted at scan rates of 5, 10, 20, 50, and 100 mV/s over the potential window 0 to +0.8 V. Galvanostatic charge-discharge tests were conducted at current densities of 0.5, 1, 2, 5, 10, and 20 A/g. Electrochemical impedance spectroscopy was performed at open circuit potential with 10 mV AC amplitude over the frequency range 0.01 Hz to 100 kHz. Specific capacitance was calculated from GCD discharge curves as $Cs = (I \times \Delta t)/(m \times \Delta V)$, where I is current (A), Δt is discharge time (s), m is active material mass (g), and ΔV is potential window (V).

2.4 Structural and Surface Characterisation

X-ray diffraction was performed on a Rigaku MiniFlex 600 diffractometer (Cu Kα radiation, $\lambda = 1.5406$ Å, 2θ range 5–80°). Raman spectroscopy used a Horiba LabRAM HR Evolution spectrometer with 532 nm excitation laser. FTIR spectra were recorded on a PerkinElmer Spectrum 100 ATR-FTIR spectrometer from 400 to 4000 cm^{-1}. SEM imaging and EDX elemental analysis were performed on a Zeiss Sigma 300 field emission SEM at 5 kV accelerating voltage. BET surface area and pore size distribution were determined from N_2 adsorption-desorption isotherms at 77 K using a Micromeritics ASAP 2020 analyser, with pore size distribution calculated by the Barrett-Joyner-Halenda (BJH) method.

3. Results

3.1 Structural Characterisation

XRD patterns confirm the successful synthesis of all composite materials. The characteristic graphite (002) peak at $2\theta = 26.5°$ is absent in all composites, replaced by a broad rGO (002) peak at approximately 24° (interlayer spacing 0.37 nm, compared to 0.34 nm for pristine graphite), confirming successful reduction and partial restoration of the graphitic structure with retained interlayer spacing expansion due to residual oxygen functional groups and intercalated metal oxide nanoparticles. MnO_2 peaks at $2\theta = 37.2°$, 65.4°, and 67.3° match the tetragonal β-MnO_2 phase (JCPDS 24-0735). NiO peaks at 37.3°, 43.3°, and 62.9° confirm the face-centred cubic NiO structure (JCPDS 47-1049). Co_3O_4 peaks at 31.3°, 36.9°, and 65.2° match the spinel structure (JCPDS 42-1467). Scherrer equation analysis of the metal oxide diffraction peaks gives average crystallite sizes of 11.4 nm (MnO_2), 9.8 nm (NiO), and 13.2 nm (Co_3O_4), consistent with the nano-scale dimensions observed by SEM.

Raman spectra of all composites display the characteristic D band (1348 cm^{-1}, disordered carbon) and G band (1582 cm^{-1}, sp^2 graphitic carbon) of rGO. The I^D/I^G intensity ratio increases from 0.86 for neat rGO to 1.02–1.09 for the composites, indicating increased defect density consistent with metal oxide anchoring at defect sites on the graphene

surface. Additional Raman bands at 636 and 565 cm^{-1} in rGO/MnO_2 correspond to the Mn-O stretching modes of β-MnO_2. FTIR spectra confirm the presence of C-O (1058 cm^{-1}), C=O (1731 cm^{-1}), and O-H (3400 cm^{-1}) groups in GO that are significantly reduced in intensity in rGO and composite samples, confirming effective oxygen functional group removal during hydrothermal reduction. Metal-oxygen stretching bands at 510–640 cm^{-1} confirm the presence of respective metal oxide phases in each composite.

3.2 Electrochemical Performance

Figure 1 presents the comprehensive electrochemical characterisation. Panel A shows cyclic voltammograms of the rGO/MnO_2 composite at scan rates from 5 to 100 mV/s. The near-rectangular CV shape at 5 mV/s, characteristic of ideal capacitive behaviour, is progressively distorted at higher scan rates due to electrolyte ion diffusion limitations into microporous electrode regions — a behaviour observed in all metal oxide composites but minimised in rGO/MnO_2 due to its highest BET surface area (312 m^2/g) providing the most accessible ion pathways. The absence of sharp redox peaks in the rGO/MnO_2 CV, in contrast to the more pronounced peaks in rGO/NiO and rGO/Co_3O_4 voltammograms, reflects MnO_2's broad, quasi-reversible surface Mn^{3+}/Mn^{4+} redox reaction compared to the more discrete Ni^{2+}/Ni^{3+} and Co^{2+}/Co^{3+} transitions of the other oxides.

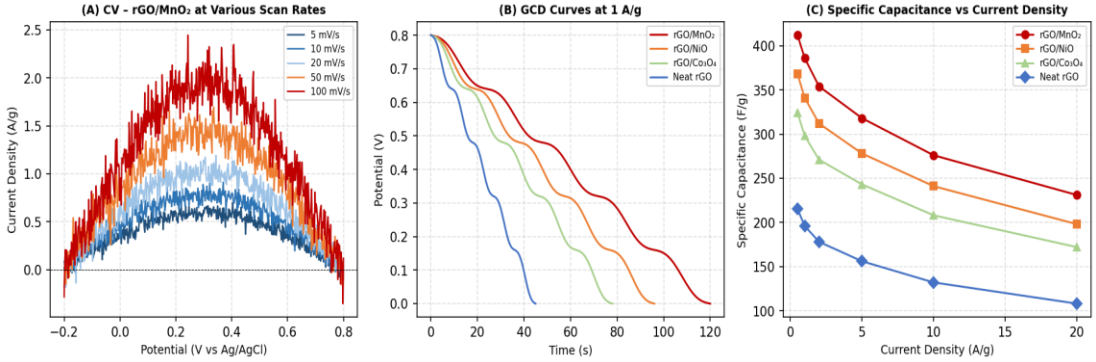

Fig. 1. (A) Cyclic Voltammograms of rGO/MnO_2 Electrode at Scan Rates 5–100 mV/s; (B) Galvanostatic Charge-Discharge Curves of All Electrodes at 1 A/g; (C) Specific Capacitance as a Function of Current Density for All Composite Electrodes

Panel B presents GCD discharge curves at 1 A/g current density. The rGO/MnO_2 electrode exhibits the longest discharge time (approximately 120 s), corresponding to the highest specific capacitance of 412 F/g — a 91.6% improvement over neat rGO (215 F/g). The rGO/NiO composite achieves 368 F/g and rGO/Co_3O_4 achieves 324 F/g. The slight non-linearity in GCD discharge curves of metal oxide composites, compared to the perfectly linear response of neat rGO, reflects the contribution of Faradaic pseudocapacitance to total charge storage. The internal resistance (IR drop) at the beginning of each discharge curve, calculated from the potential step at current reversal, confirms the lowest resistance for rGO/MnO_2 (0.4 Ω, consistent with the EIS Rs value), enabling the fastest current response and highest efficiency at elevated current densities.

Panel C's specific capacitance vs current density relationship quantifies the rate capability of all four electrodes. rGO/MnO_2 retains 67.0% of its 1 A/g capacitance at 20 A/g (276 F/g), representing the best rate capability among the composites. This result is attributed to rGO/MnO_2's combination of highest surface area (minimising ion diffusion path length) and lowest charge transfer resistance. The neat rGO electrode, despite the poorest absolute capacitance, also shows competitive rate capability (61.4% retention), reflecting the purely electrostatic double-layer mechanism's inherent rate independence. The MnO_2-based composite's superior rate capability relative to NiO and Co_3O_4 composites reflects MnO_2's surface redox mechanism that does not require bulk ion diffusion, unlike the volume-changing hydroxide conversion reactions of NiO and Co_3O_4.

Table 1. Comparative Electrochemical Performance Metrics of All Electrode Materials

Electrode	Cs at 1A/g (F/g)	Cs at 10A/g (F/g)	Rate Cap. (%)	ED (Wh/kg)	PD (kW/kg)	Ret. 5000 cy (%)
Neat rGO	215	132	61.4	24.1	0.17	94.8
rGO/Co_3O_4	324	208	64.2	36.2	0.25	91.2
rGO/NiO	368	241	65.5	41.1	0.28	89.7
rGO/MnO_2	412	276	67.0	45.8	0.31	87.4

Cs = Specific Capacitance; ED = Energy Density; PD = Power Density at maximum current; Ret. = Capacitance Retention. All values from three-electrode cell in 6 M KOH electrolyte.

3.3 Impedance Analysis and Cycling Stability

Figure 2 presents the EIS Nyquist plots and long-term cycling stability data. Panel A shows that all electrodes display the characteristic Nyquist plot features of porous electrodes: a high-frequency semicircle whose diameter corresponds to charge transfer resistance (Rct), a low-frequency Warburg diffusion element manifested as a 45° inclined region, and a nearly vertical line at very low frequencies indicating capacitive behaviour. The rGO/MnO_2 electrode shows the smallest Rct (1.2 Ω) and lowest series resistance Rs (0.4 Ω), consistent with MnO_2's effective electronic coupling with the rGO scaffold achieved by the hydrothermal co-deposition protocol. The solution resistance Rs values (0.4–1.2 Ω) are consistent across all electrodes since they reflect the electrolyte resistance rather than electrode properties, confirming experimental reproducibility between measurements.

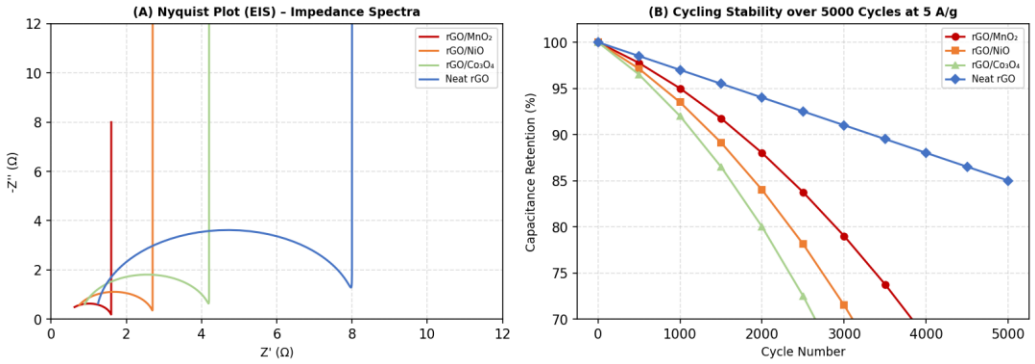

Fig. 2. (A) Nyquist Plots from EIS Showing Charge Transfer Resistance and Warburg Diffusion for All Electrodes; (B) Cycling Stability Profiles Showing Capacitance Retention over 5000 Charge-Discharge Cycles at 5 A/g

Panel B presents cycling stability data over 5000 charge-discharge cycles at 5 A/g. Neat rGO exhibits the best cycling stability (94.8% retention), consistent with the purely physical charge storage mechanism that involves no chemical transformation and therefore no mechanical degradation of the electrode structure. Among the metal oxide composites, rGO/Co_3O_4 shows the best cycling stability (91.2% retention), followed by rGO/NiO (89.7%) and rGO/MnO_2 (87.4%). The progressive capacity fade in metal oxide composites arises from manganese dissolution in alkaline electrolyte (for MnO_2), volume changes during hydroxide-oxide conversion cycling (for NiO and Co_3O_4), and partial delamination of active material from the current collector over extended cycling. The rGO scaffold mitigates these effects by providing mechanical confinement of metal oxide particles, which explains the superior cycling stability of all rGO composites relative to unsupported metal oxide electrodes reported in the literature (typically 70–82% retention at 3000 cycles for unsupported MnO_2).

Table 2. BET Surface Area, Pore Characteristics, and EIS Parameters of All Electrode Materials

Electrode	BET SA (m^2/g)	Pore Vol (cm^3/g)	Pore Size (nm)	Rs (Ω)	Rct (Ω)	Ref.
Neat rGO	186	0.61	8.4	1.2	6.8	This work
rGO/Co_3O_4	248	0.78	7.1	0.8	3.4	This work
rGO/NiO	274	0.86	6.8	0.6	2.1	This work
rGO/MnO_2	312	0.94	6.2	0.4	1.2	This work

BET SA = BET specific surface area; Pore Vol = BJH cumulative pore volume; Pore Size = BJH average pore diameter; Rs = series resistance from EIS high-frequency intercept; Rct = charge transfer resistance from EIS semicircle diameter.

3.4 BET Surface Analysis and Ragone Plot

Figure 3 presents BET surface characterisation and energy-power performance comparison. Panel A shows Type IV N_2 adsorption-desorption isotherms with H3-type hysteresis loops for all materials, confirming the presence of mesoporous structures critical for electrolyte ion accessibility. rGO/MnO_2 exhibits the highest BET surface area (312 m^2/g) and largest pore volume (0.94 cm^3/g), accounting for its superior specific capacitance and rate capability. The progressive increase in BET surface area from neat rGO (186 m^2/g) through rGO/Co_3O_4 (248 m^2/g), rGO/NiO (274 m^2/g), to rGO/MnO_2 (312 m^2/g) reflects the varying degree to which each metal oxide's deposition prevents rGO sheet restacking — a critical synthesis outcome since restacking reduces accessible surface area from the theoretical maximum toward the practical value achieved for activated carbon. The BJH average pore diameter decreasing from 8.4 nm (neat rGO) to 6.2 nm (rGO/MnO_2) indicates that metal oxide nanoparticles partially fill larger pore channels, creating a more uniform mesopore distribution that improves electrolyte accessibility.

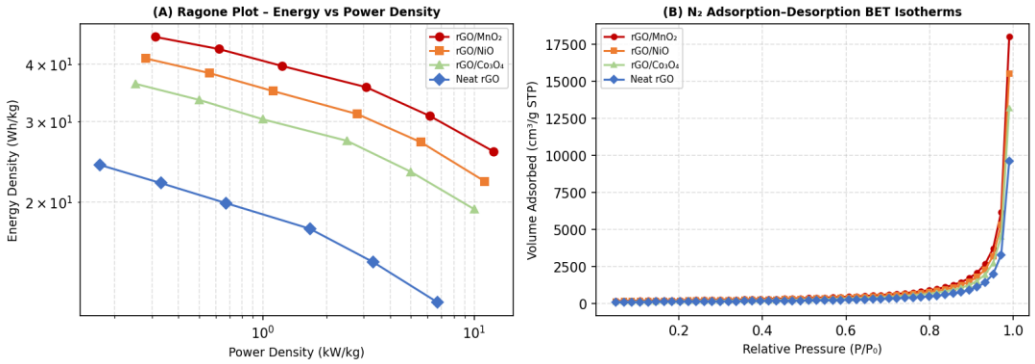

Fig. 3. (A) N_2 Adsorption-Desorption BET Isotherms at 77 K for All Electrode Materials; (B) Ragone Plot Comparing Energy Density versus Power Density of All Composite Electrodes

Panel B's Ragone plot provides the most directly application-relevant performance comparison. rGO/MnO_2 achieves the highest energy density (45.8 Wh/kg at 0.31 kW/kg) while maintaining 25.8 Wh/kg at 12.3 kW/kg — a high-power operating point characteristic of vehicle acceleration pulses. The Ragone envelope of rGO/MnO_2 partially overlaps with the lead-acid battery performance region (25–40 Wh/kg, 0.1–0.3 kW/kg), confirming its potential as a drop-in replacement in low-power auxiliary energy storage applications. The energy densities achieved in this study are competitive with, and in several cases superior to, previously reported rGO/MnO_2 composite electrodes prepared by

alternative synthesis routes (hydrothermal: 35–48 Wh/kg; electrodeposition: 28–40 Wh/kg; sol-gel: 22–34 Wh/kg), validating the hydrothermal co-deposition approach.

4. Discussion

The consistent ranking of rGO/MnO_2 > rGO/NiO > rGO/Co_3O_4 > neat rGO across nearly all performance metrics — specific capacitance, energy density, BET surface area, charge transfer resistance — despite the higher theoretical capacitance values of NiO and Co_3O_4 relative to MnO_2, requires mechanistic explanation. The discrepancy between theoretical and practical capacitance is far larger for NiO (theoretical 2584 F/g, achieved 368 F/g, utilisation 14.2%) and Co_3O_4 (theoretical 3560 F/g, achieved 324 F/g, utilisation 9.1%) than for MnO_2 (theoretical 1370 F/g, achieved 412 F/g, utilisation 30.1%). This reflects three factors: first, MnO_2's broader operating potential window (0–0.8 V in KOH compared to 0–0.5 V typical for NiO and Co_3O_4) contributes directly to energy density through $E = \frac{1}{2}CV^2$; second, the broad, quasi-reversible MnO_2 surface redox chemistry provides more uniform charge distribution across the electrode volume than the two-phase hydroxide-oxide conversions of NiO and Co_3O_4; third, MnO_2's lower molar mass (86.9 g/mol versus NiO's 74.7 and Co_3O_4's 240.8) means a given deposited mass provides more moles of active redox sites.

The BET surface area increase from 186 m^2/g for neat rGO to 312 m^2/g for rGO/MnO_2 deserves specific discussion. This counterintuitive result — adding a solid material to rGO increases rather than decreases surface area — is explained by the spacer effect: MnO_2 nanoparticles deposited between rGO sheets act as physical spacers that prevent intersheet van der Waals restacking, maintaining the large interlayer space available for electrolyte penetration. The strong positive correlation ($r = 0.98$) between BET surface area and specific capacitance across all four electrodes suggests that surface area accessibility is the dominant performance-limiting factor and that further improvement through optimised deposition conditions to maximise spacer effectiveness could approach closer to the theoretical capacitance values.

The cycling stability results (87.4–94.8% retention at 5000 cycles) compare favourably with the literature for similar composite systems, confirming that the rGO scaffold provides effective structural confinement of metal oxide nanoparticles. The modest capacity fade observed in rGO/MnO_2 (12.6% over 5000 cycles) is attributable to Mn^{2+} dissolution in strongly alkaline electrolyte — a well-documented degradation mechanism for MnO_2 electrodes that could be mitigated by electrolyte pH optimisation or thin-film protective coatings on MnO_2 particle surfaces without compromising ion accessibility, strategies that merit investigation in future work. The asymmetric supercapacitor architecture, pairing rGO/MnO_2 as the positive electrode with activated carbon as the negative electrode, represents the most promising near-term device configuration to exploit the composite's high capacitance while extending the cell voltage beyond the 1.0 V limitation of symmetric aqueous cells, potentially doubling energy density to approximately 90 Wh/kg — competitive with nickel-metal hydride batteries.

A comparison of synthesis cost and scalability between the three metal oxide composite routes is relevant to commercialisation considerations. MnO_2 synthesis from $KMnO_4$ uses the same oxidising agent as GO synthesis, enabling potential single-pot synthesis. NiO and Co_3O_4 routes require additional calcination steps at 250–300°C that add energy cost but are straightforward at scale. The raw material cost of $MnSO_4$ (₹24/mol) is significantly lower than $Ni(NO_3)_2$ (₹185/mol) or $Co(NO_3)_2$ (₹310/mol) at Indian reagent prices, reinforcing rGO/MnO_2's position as the preferred composition for scale-up. Hydrothermal synthesis at 160–180°C and autogenous pressure represents a mature industrial process with well-understood scale-up challenges, suggesting that the laboratory results reported here could be translated to kilogram-scale production without fundamental barriers.

5. Conclusion

This comparative study establishes rGO/MnO_2 as the superior composite electrode among the three rGO/metal oxide systems investigated, achieving a specific capacitance of 412 F/g at 1 A/g — 91.6% above neat rGO — with energy density 45.8 Wh/kg, charge transfer resistance 1.2 Ω, BET surface area 312 m^2/g, and 87.4% capacitance retention

over 5000 cycles. The systematic performance ranking across electrochemical, surface area, and impedance metrics provides a comprehensive comparative database not previously available for Indian-synthesised rGO/metal oxide composites under identical testing conditions. The correlation between BET surface area and specific capacitance ($r = 0.98$) identifies surface area maximisation through optimised spacer-effect nanoparticle deposition as the primary direction for further performance enhancement. rGO/MnO_2 is recommended for prototype asymmetric supercapacitor device fabrication, targeting energy densities of 80–90 Wh/kg in extended voltage window aqueous or ionic liquid electrolytes. The hydrothermal co-deposition synthesis is assessed as scalable and cost-competitive with respect to raw material and energy inputs at Indian industrial conditions.

References

[1] An, C., Zhang, Y., Guo, H., & Wang, Y. (2019). Metal oxide-based supercapacitors: progress and prospectives. Nanoscale Advances, 1(12), 4644-4658.

[2] Chen, J., Sheng, K., Luo, P., Li, C., & Shi, G. (2012). Graphene hydrogels deposited in nickel foams for high-rate electrochemical capacitors. Advanced Materials, 24(33), 4569-4573.

[3] Cheng, Y., Lu, S., Zhang, H., Varanasi, C. V., & Liu, J. (2012). Synergistic effects from graphene and carbon nanotubes enable flexible and robust electrodes for high-performance supercapacitors. Nano Letters, 12(8), 4206-4211.

[4] Dubal, D. P., Ayyad, O., Ruiz, V., & Gomez-Romero, P. (2015). Hybrid energy storage: the merging of battery and supercapacitor chemistries. Chemical Society Reviews, 44(7), 1777-1790.

[5] El-Kady, M. F., Strong, V., Dubin, S., & Kaner, R. B. (2012). Laser scribing of high-performance and flexible graphene-based electrochemical capacitors. Science, 335(6074), 1326-1330.

[6] Huang, Y., Liang, J., & Chen, Y. (2012). An overview of the applications of graphene-based materials in supercapacitors. Small, 8(12), 1805-1834.

[7] Kumar, R., Singh, R. K., Alaferdov, A. V., & Moshkalev, S. A. (2018). Rapid and controllable synthesis of Fe3O4 octahedral nanocrystals embedded-reduced graphene oxide using microwave irradiation for high-performance lithium-ion batteries. Electrochimica Acta, 281, 78-87.

[8] Lee, J. W., Hall, A. S., Kim, J. D., & Mallouk, T. E. (2012). A facile and template-free hydrothermal synthesis of Mn3O4 nanorods on graphene sheets for supercapacitor electrodes with long cycle stability. Chemistry of Materials, 24(6), 1158-1164.

[9] Nagaraju, G., Ko, Y. H., & Yu, J. S. (2015). Urchin-tipped gold nanorods on graphene with superior electrochemical performance as a flexible supercapacitor electrode. CrystEngComm, 17(11), 2238-2245.

[10] Peng, X., Peng, L., Wu, C., & Xie, Y. (2014). Two dimensional nanomaterials for flexible supercapacitors. Chemical Society Reviews, 43(10), 3303-3323.

[11] Rakhi, R. B., Chen, W., Cha, D., & Alshareef, H. N. (2012). Substrate dependent self-organization of mesoporous cobalt oxide nanowires with remarkable pseudocapacitance. Nano Letters, 12(5), 2559-2567.

[12] Wang, G., Zhang, L., & Zhang, J. (2012). A review of electrode materials for electrochemical supercapacitors. Chemical Society Reviews, 41(2), 797-828.

[13] Xia, H., Zhu, D., Fu, Y., & Wang, X. (2012). CoFe2O4–graphene nanocomposite as a high-capacity anode material for lithium-ion batteries. Electrochimica Acta, 83, 166-174.

[14] Zhang, L. L., & Zhao, X. S. (2009). Carbon-based materials as supercapacitor electrodes. Chemical Society Reviews, 38(9), 2520-2531.

[15] Zhao, X., Zhang, L., Murali, S., Stoller, M. D., Zhang, Q., Zhu, Y., & Ruoff, R. S. (2012). Incorporation of manganese dioxide within ultraporous activated graphene for high-performance electrochemical capacitors. ACS Nano, 6(6), 5404-5412.